UC Berkeley
UC Berkeley Previously Published Works

Title
Tilted fluctuation electron microscopy

Permalink
https://escholarship.org/uc/item/73c5w99j

Journal
Applied Physics Letters, 117(9)

ISSN
0003-6951

Authors
Kennedy, Ellis
Reynolds, Neal
DaCosta, Luis Rangel
et al.

Publication Date
2020-08-31

DOI
10.1063/5.0015532

Peer reviewed

eScholarship.org Powered by the California Digital Library
University of California

Applied Physics Letters

Tilted fluctuation electron microscopy

Cite as: Appl. Phys. Lett. **117**, 091903 (2020); https://doi.org/10.1063/5.0015532
Submitted: 29 May 2020 . Accepted: 19 August 2020 . Published Online: 01 September 2020

Ellis Kennedy, Neal Reynolds, Luis Rangel DaCosta, Frances Hellman, Colin Ophus, and M. C. Scott

ARTICLES YOU MAY BE INTERESTED IN

Study of dislocations in AlN single-crystal using bright-field synchrotron x-ray topography under a multiple-beam diffraction condition
Applied Physics Letters **117**, 092102 (2020); https://doi.org/10.1063/5.0015108

Broadband operation of active terahertz quarter-wave plate achieved with vanadium-dioxide-based metasurface switchable by current injection
Applied Physics Letters **117**, 091102 (2020); https://doi.org/10.1063/5.0019265

Lanthanum doping induced structural changes and their implications on ferroelectric properties of $Hf_{1-x}Zr_xO_2$ thin film
Applied Physics Letters **117**, 092902 (2020); https://doi.org/10.1063/5.0021007

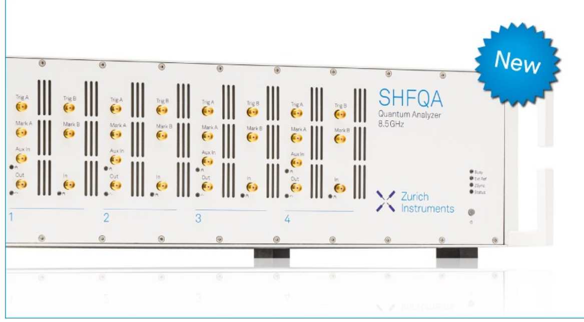

Your Qubits. Measured.
Meet the next generation of quantum analyzers
- Readout for up to 64 qubits
- Operation at up to 8.5 GHz, mixer-calibration-free
- Signal optimization with minimal latency
Find out more

© 2020 Author(s).

Tilted fluctuation electron microscopy

Cite as: Appl. Phys. Lett. **117**, 091903 (2020); doi: 10.1063/5.0015532
Submitted: 29 May 2020 · Accepted: 19 August 2020 ·
Published Online: 1 September 2020

View Online

Export Citation

CrossMark

Ellis Kennedy,[1] Neal Reynolds,[2,3] Luis Rangel DaCosta,[4] Frances Hellman,[1,2,3] Colin Ophus,[4] and M. C. Scott[1,4,a)]

AFFILIATIONS

[1]Department of Materials Science and Engineering, University of California Berkeley, Berkeley, California 94720, USA
[2]Department of Physics, University of California Berkeley, Berkeley, California 94720, USA
[3]Materials Science Division, Lawrence Berkeley National Laboratory, Berkeley, California 94720, USA
[4]NCEM, Molecular Foundry, Lawrence Berkeley National Laboratory, Berkeley, California 94720, USA

[a)]Author to whom correspondence should be addressed: mary.scott@berkeley.edu

ABSTRACT

Fluctuation electron microscopy (FEM) is a scanning nanodiffraction-based method that offers a unique approach to characterizing nanometer-scale medium-range order (MRO) in disordered materials. In addition to determining the degree of MRO, careful analysis of scanning nanodiffraction data can also be used to determine strain in thin film amorphous samples. We applied FEM to characterize the strain and MRO of magnetron sputtered amorphous tantalum (*a*-Ta) thin films over a range of tilt angles from 0° to 45° in order to measure any deviations between the in-plane and out-of-plane strain and MRO. We validate our approach using electron diffraction simulations of FEM experiments for *a*-Ta. We measure anisotropic strain in the simulated *a*-Ta diffraction patterns and find that the experimental *a*-Ta is isotropically strained within the accuracy of our method. Our approach provides a workflow for acquiring tilted scanning nanodiffraction data, determining the relative strain and ordering as a function of in- and out-of-plane directions, and removing any artifacts induced in FEM data due to strain. We also describe some limitations of the tilted FEM method when applied to thin films with very low strains.

© 2020 Author(s). All article content, except where otherwise noted, is licensed under a Creative Commons Attribution (CC BY) license (http://creativecommons.org/licenses/by/4.0/). https://doi.org/10.1063/5.0015532

Thin amorphous films are technologically important for applications such as antireflective coatings,[1] stabilizing coatings for battery materials,[2] and in electronic devices.[3] Although amorphous materials lack long-range crystalline order, they contain structural correlations on the scale of a few nanometers, known as medium-range order (MRO). Aspects of amorphous materials such as mechanical behavior and electronic properties are thought to depend on the degree of MRO in the material.[4–6] To accurately understand the relationship between the structure and properties in thin amorphous films, it is necessary to measure both MRO and effects of thin film deposition, such as strain induced by substrate interaction and deposition conditions.

While pair distribution functions can be measured and average bond lengths calculated using various experimental methods, the MRO and its distribution on the scale of 1–4 nm are difficult to measure. X-ray and neutron diffraction and Raman spectroscopy are commonly used for strain characterization but cannot provide information on such small length scales.[7,8] Fluctuation electron microscopy (FEM) is uniquely sensitive to the relative degree of ordering on this length scale and can measure MRO across samples and regions of a sample.[9] To be sensitive to MRO, we converge the electron beam in the sample plane, generating a probe that is approximately 2 nm in diameter and is sensitive to MRO on a similar length scale. When implemented in scanning transmission electron microscopy (STEM), FEM collects many diffraction patterns at different probe positions. Electrons passing through a thin material are kinematically scattered according to the sample's atomic structure.[10] When ordering exists, atom clusters oriented near a diffraction angle producing constructive interference will result in a peak in the diffraction pattern. To determine relative MRO, the mean variance of the diffraction patterns is calculated as a function of scattering vector, averaged across probe positions. Past research used FEM to relate MRO and shear band kinetics in metallic glasses[11] and to elucidate the distribution of MRO configurations in amorphous Zr–Cu films.[12]

MRO is typically assumed to be isotropic. While some studies considered anisotropy in short-range order by calculating tilted radial distribution functions,[13,14] no studies have considered anisotropic MRO. In contrast, relative out-of-plane strain is nearly ubiquitous in deposited thin films and strongly affects the mechanical, electrical, and other properties of the films.[15] In amorphous films, strain can also affect properties and performance.[16–18] The same nanodiffraction

© Author(s) 2020

patterns used for measuring MRO in FEM analysis can be used to determine strain in thin amorphous films.[19–22]

To measure the degree of MRO in the in- and out-of-plane directions, we developed an FEM protocol that accounts for the effects of strain, which could otherwise reduce the accuracy of FEM variance curves. We applied this to experimental and theoretical data from a series of FEM scans at varying tilt angles, with the goal of measuring the in- and out-of-plane degrees of MRO and strain.

This work implements a scanning nanodiffraction experimental setup and a data processing pipeline to extract directional structural information from thin amorphous films. To interpret data obtained from strained materials at various tilt angles, it is necessary to decouple the effects of strain and changing MRO on the FEM data. To achieve this, we developed mathematical methods to accurately fit the elliptical electron diffraction data to decouple imperfections in microscope alignment and the effects of strain in FEM data. We then corrected for both and calculated accurate FEM variance curves from the tilted data. This method was tested on simulated strained amorphous tantalum (*a*-Ta) and showed the ability to recover the accurate isotropic MRO as well as measure the relative degree of strain in the in- and out-of-plane directions. We also applied our method to experimental deposited *a*-Ta data that is isotropic to the precision of our measurement.

a-Ta films capped with amorphous SiN_x (a-SiN_x) were deposited onto a-SiN_x substrates using magnetron sputtering. Both *a*-Ta and a-SiN_x were sputtered at room temperature in 1 mTorr of Ar pressure under a base pressure of 7×10^{-8} Torr at growth rates of 0.25 Å/s and 0.05 Å/s, respectively. The films were deposited on 10 nm thick Norcada a-SiN_x grids with nine 0.1 mm × 0.1 mm windows. Samples consisted of an 8 nm *a*-Ta film capped with 10 nm of a-SiN_x to prevent oxidation. Additionally, a control sample of 10 nm of a-SiN_x was deposited to determine the influence of the capping layer on the variational data. The observed uniform speckle pattern and *a*-Ta mean diffraction pattern confirmed that the films were amorphous.

Experiments were carried out in an FEI Titan operated at an acceleration voltage of 200 kV. The third condenser lens current was set such that the convergence angle was 0.51 mrad, resulting in a measured 2.2 nm diameter probe and a 15.5 pA probe current. Images were collected on an Orius CCD system with an exposure time of 0.3 s and a camera length of 300 mm. The images were binned by a factor of four to a final size of 512 × 512 pixels. Nanodiffraction data were collected as 12 × 12 image stacks (144 total images) for each tilt with 5 nm step sizes between regions of analysis. A beam stop covered the central beam and the beam remained in the same location in all FEM images. For both samples, data were collected at tilts of 0°, 15°, 30°, and 45°. Collection was repeated four times per tilt angle (576 images per angle) for statistical averaging and over different regions of the film to avoid excess contamination. There was negligible variation between data from different locations on a single film at a set tilt angle. During the experiment, all diffraction patterns were taken with the same imaging conditions to ensure that the effects of microscope misalignment were the same across all patterns.

The simulated *a*-Ta atomic structure was computed from molecular dynamics Large-scale Atomic/Molecular Massively Parallel Simulator (LAAMPS) simulations provided by Ding *et al.*[23] The simulated *a*-Ta structure was tilted, rotated to a random angle, distorted using a 3D strain tensor, and then cropped to the simulation cell size. A compressive strain of −2% was applied to the simulated *a*-Ta structure in the two in-plane directions, and a tensile strain of +1.2% was applied in the out-of-plane direction (i.e., we assume a Poisson's ratio of 0.3). Simulations of electron diffraction from simulated *a*-Ta were performed using the multislice method implemented in the Prismatic code with methods following Ophus[24] and Pryor *et al.*[25] The simulation FEM parameters were chosen to match the FEM experiment described above, with the geometry shown in Fig. 1. The simulated probe was just under 2 nm in diameter[26] for a convergence angle of 0.51 mrad. A step size of 2 nm avoided overlapping measurements. A total of 676 probe positions were collected for each of ten tilt angles, from 0° to 45° in increments of 5°. The inset in Fig. 1 is a diagram of how the sample is tilted about the x-axis. Data were collected from a 52 nm × 52 nm region (26 × 26 probe positions) of the simulated *a*-Ta film. Sixteen frozen phonon configurations were used in the simulation. A pixel size of 0.15 Å was used, giving a maximum scattering angle of 42 mrads. Figure 1 shows a single representative diffraction image from the 0° and 45° tilt data and the summed 0° and 45° tilt data stacks. For each tilt, the patterns were summed to form a mean image for alignment and measurement of the mean strain.

Radial fitting of the mean scanning nanodiffraction image at each tilt used least squares fitting of the first ring, implemented in Matlab, following a procedure similar to the one used by Gammer *et al.*[19] The script uses initial parameters as a rough guess to fit the amorphous ring intensity and then refines the fit to accurately determine these parameters. The fitting parameters for the diffracted ring are the center coordinates, two elliptical fitting coefficients, intensity outside of the first ring (to account for a constant background), intensity between the center and the first ring, ring width, and radius. The scripts are accessible on GitHub.[27]

After radial fitting of the mean diffraction data, we used the two elliptical fitting coefficients to determine strain and mean variation intensity. The approach to preparing data for both types of analysis is as follows: first, we calculated strain values for all the data based on the elliptical fitting coefficients as described below. Since it is possible that

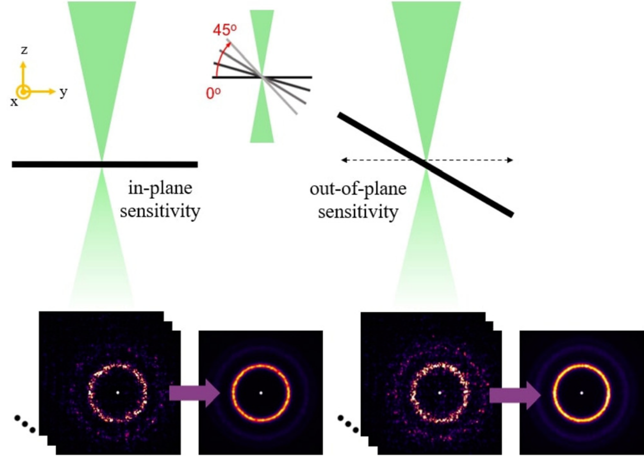

FIG. 1. Setup for tilted FEM analysis of *a*-Ta. A converged electron beam was rastered across the sample at different tilt angles. The sample is tilted with respect to the beam with the x-axis fixed. The dotted line indicates the plane probed for MRO. Individual and summed scanning nanodiffraction images are shown for the simulated *a*-Ta film tilted to 0° (left) and 45° (right).

© Author(s) 2020

projector lens distortions also induce ellipticity in the diffraction patterns, we considered the 0° pattern to have zero in-plane strain and eliminated the contribution of any projector lens distortion by subtracting off the measured 0° strain values for all the data. The variational intensity as a function of **k** vector at each tilt angle was calculated from scanning nanodiffraction data after all ellipticity had been removed. We first applied this method to simulated data to ensure that the correct out-of-plane strain value was recovered. After validating our method on the simulated data, we applied it to the diffraction data from the experimentally deposited *a*-Ta, which was in an unknown strain state.

Relative strain was determined by the mapping of a circle into a fitted ellipse. A detailed description of the strain fitting procedure is given by Gammer *et al.*[19] and Savitzky *et al.*[28] Nanodiffraction is most sensitive to bond lengths that lie in the plane perpendicular to the beam. When the sample is tilted, this plane includes bond lengths in the out-of-plane sample direction. If these bond lengths are different, the circular diffraction pattern will be distorted into an ellipse. By fitting this ellipse and accounting for the projected distortion of the tilted sample's diffraction pattern, the degree of relative out-of-plane strain can be determined. Strain in the y-z plane along the z′- direction is ε_{zz} and strain in the x′-direction along the x-axis is ε_{xx}. The ε_{xz} strain bisects the x′ and z′ vectors. The x′-direction is the in-plane direction that remains constant and the z′-direction is the out-of-plane direction that provides information about relative strain.

Figure 2 shows the measured strain as a function of tilt angle for the experimental and simulated *a*-Ta films. The experimental *a*-Ta film exhibited no trend with the tilt angle, while the simulated *a*-Ta film showed an increase in strain from 0 to approximately 2% as the tilt angle was varied from 0° to 45°. This workflow detected the induced strain in the simulated *a*-Ta structure, shown in Fig. 2(b). For the simulated data, the maximum theoretical relative strain is 3.2% ($\varepsilon_{zz}(\theta) = 3.2 \times \sin^2(\theta)$), which would be reached at a tilt of 90° (experimentally inaccessible), shown as the green dashed line in Fig. 2. This theoretical relationship is derived from considering infinitesimal strain in rotated coordinates.[29] The green dashed line in Fig. 2 indicates the theoretical strain along the ε_{zz} direction as a function of tilt angle for the simulated *a*-Ta data, which is in good agreement with the measurement for the measured tilt values.

As illustrated in Fig. 1, the x-oriented strain (ε_{xx}) is perpendicular to the tilt axis and remains constant as a function of tilt angle. Because ε_{xx} is constant across tilt angles, the relative strain compared to the zero-tilt condition is approximately zero for all tilts. Based on our ε_{xx} and ε_{xz} strain values and their deviations from zero relative strain, the precision of the strain measurement is approximately 0.2%. As shown in Fig. 2(a), the experimental *a*-Ta strain values are below this threshold, confirming that the experimental *a*-Ta sample is isotropic to within our measurement's sensitivity.

Variational analysis was also carried out to determine the feasibility of measuring MRO in the in- and out-of-plane directions. To do this, each diffraction pattern for a given tilt angle was first elliptically corrected based on the elliptical fit of the average diffraction pattern. This removed any ellipticity in the diffraction patterns due to either microscope misalignment or strain. The variance as a function of scattering vector was calculated for the four tilt angles, 0°, 15°, 30°, and 45°. The normalized variance, $V(k)$, was calculated as[30]

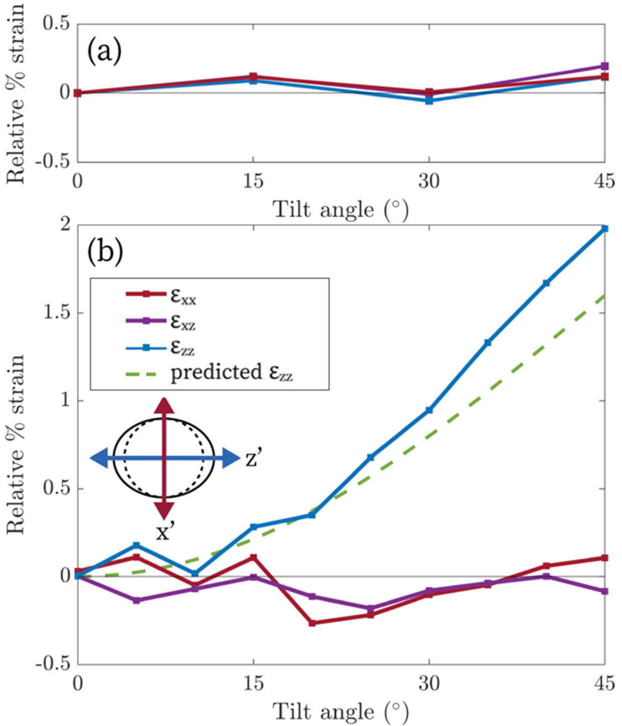

FIG. 2. (a) Strain as a function of tilt angle for the experimental *a*-Ta. Change in relative strain was below the ±0.2% margin of error, indicating that the film is strain isotropic. (b) Strain as a function of tilt angle (degrees) for simulated *a*-Ta. The 0° tilt strain is set to zero for all orientations. The z′-oriented strain changes with the tilt angle. The green dotted curve is the mathematical prediction of the z′-oriented strain as a function of tilt angle.

$$V_\sigma(\mathbf{k}) = \frac{\langle I^2(\mathbf{k}, r)\rangle - \langle I(\mathbf{k}, r)\rangle^2}{\langle I(\mathbf{k}, r)\rangle^2}, \quad (1)$$

where I is the measured intensity at the scattering vector **k** for position on the sample r. Variance curves were computed for each tilt angle following the method outlined by Hwang and Voyles,[31] in which the radial average is computed for each scanning nanodiffraction pattern to produce a single mean intensity value for each **k** and scanning nanodiffraction pattern.[31] Then, the normalized variance of the annular mean is computed from the mean patterns. The variance curves are plotted in Fig. 3 with and without strain correction for simulated *a*-Ta and with strain correction for experimental *a*-Ta.

To approximate the signal from the experimental *a*-Ta without the *a*-SiN_x capping and membrane layers, the mean *a*-SiN_x intensity for a specific tilt was subtracted from each of the experimental *a*-Ta images from that tilt angle. The intensity-corrected experimental *a*-Ta images were then analyzed using the variance computation process described above. The normalized variance curves are shown in Fig. 3. The dotted lines are the *a*-SiN_x variance signals that were subtracted to produce the solid line curves shown in the same plot.

The variance curves of the experimental *a*-Ta are compared by the peak height and the ratio of the normalized variance of peak 1 (located around 2.66 nm^{-1}) to peak 2 (located at 4.44 nm^{-1}). The peak in the variational data varies with the tilt angle. To determine whether

© Author(s) 2020

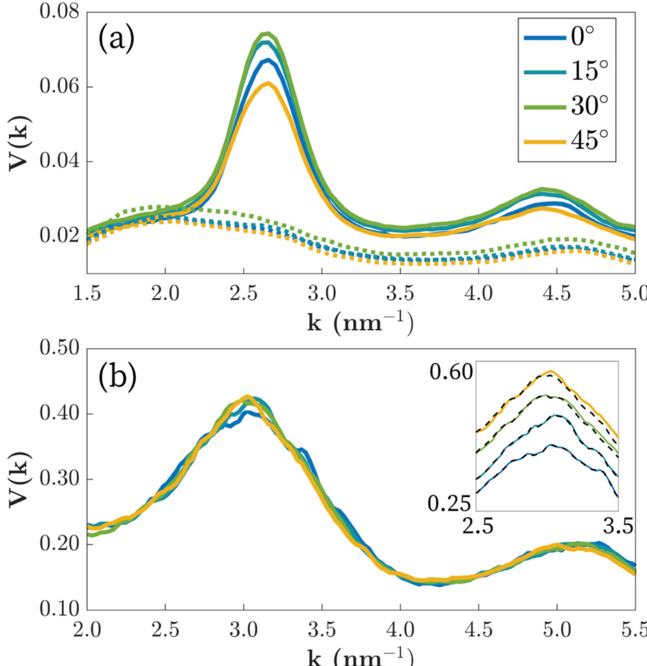

FIG. 3. Variance as a function of **k** for the (a) experimental *a*-Ta film and (b) simulated *a*-Ta structure. (a) The experimental *a*-Ta curves have had the mean *a*-SiN_x signal from the control samples *a*-Ta subtracted. The dotted lines show the *a*-SiN_x contribution that was subtracted away. The first and second peak positions differ between the experimental and simulated data by approximately 0.36 nm^{-1}. (b) The inset in the simulated data plot shows the difference between elliptically corrected and uncorrected data (black dashed lines) with a vertical offset.

this was simply a result of the effective increased film thickness due to tilting resulting in decreased variance or if multiple scattering was influencing the peak heights, we calculated the ratio between peak 1 and peak 2 and used this as a metric for the presence of inelastic scattering.[32] Table I gives the variance ratio of the first peak to the second peak and the relative percentage of the height ratio. Peak 1, corresponding to the average bond length, occurs at a scattering vector of 2.66 nm^{-1} (mean bond length of 3.76 Å) for all peaks and peak 2 occurs at a scattering vector of 4.40 nm^{-1} (2.27 Å) for tilts of 15°, 30°, and 45°, but at 4.49 nm^{-1} (2.23 Å) for a tilt of 0°. The ratio of the variance of peak 1 to the variance of peak 2 decreases with the tilt angle. Therefore, while increasing the sample thickness will decrease variational intensity in FEM measurements, it is likely that multiple scattering resulting from the increased thickness is also occurring and influencing variance peak intensity.[33] Analysis of peak 1 for each tilt

TABLE I. Variance peak height ratios for experimental *a*-Ta film.

Tilt angle (°)	Peak 1: peak 2	Relative ratio
0°	3.40	100%
15°	3.35	98.7%
30°	3.29	96.7%
45°	3.11	91.6%

shows no changing peak geometry or horizontal shift of the peak location, supporting the strain portion of the study that indicates that the experimental film is isotropic.

The simulated *a*-Ta structure with strain correction shows a similar trend to the experimental data. The average bond length of the simulated data is 3.02 nm^{-1} (3.31 Å). In Fig. 3, the data for all simulated tilts differ by 0.36 nm^{-1} from the experimental data. We attribute the difference in mean scattering vector to differences in atomic packing between the experimental and simulated Ta.

The inset in Fig. 3 shows how elliptical correction affects the variance curves in the simulated FEM data. Although we hypothesized that determining and removing the strain contributions to the FEM signal allow for more accurate calculations of variance for each stack of tilted data, there is a negligible difference between the corrected and uncorrected variance curves. We attribute this to the normalization performed in Eq. (1), which counteracts any changes due to ellipticity in the variational data. While we find no large changes in the FEM results after removing the effects of strain, elliptical corrections may be required to interpret fine features in FEM data.

In this study, we developed a protocol to measure and remove the effects of strain for accurate determination of MRO from thin film FEM data, while being sensitive to differences in bond lengths in the in- vs out-of-plane directions. Our workflow accounts for any changes in MRO due to structural anisotropy in bond lengths in a deposited thin film. We observe that multiple scattering influences variational peak height in an unpredictable manner. We also demonstrated, in simulated data, the ability to measure relative out-of-plane strain in thin films from scanning nanodiffraction data and establish a sensitivity limit of ±0.2% relative strain for our data, likely a result of the low signal-to-noise ratio of the amorphous diffraction rings. For this reason, other methods are required to measure small changes in the average bond length in the in- vs out-of-plane directions for these films. Using these methods, we determined that any differences in the in- and out-of-plane strains in the experimental *a*-Ta were below the level of sensitivity of our method. For the experimental *a*-Ta, changes in the MRO as a function of tilt angle are obscured by effects of changing thickness and diffracted intensity. However, the variance curves show consistent peak features across all tilt angles, indicating that the average bond length of the MRO is consistent across the measured tilts. Through the combined analysis of simulated and experimental *a*-Ta, this work provides a method for accounting for ellipticity in variance calculations and measuring relative change in strain as a function of orientation within a film.

This work was supported by National Science Foundation STROBE Grant No. DMR-1548924. The work at the Molecular Foundry was supported by the Office of Science, Office of Basic Energy Sciences, of the U.S. Department of Energy under Contract No. DE-AC02-05CH11231. Growth and nonelectron microscopy characterization of experimental *a*-Ta and *a*-SiN_x were performed by N.R. and supported by the U.S. Department of Energy, Office of Science, Basic Energy Sciences, Materials Sciences and Engineering Division under Contract No. DE-AC02-05-CH11231, under the Nonequilibrium Magnetic Materials Program (No. KC2204). We thank Karen Bustillo for her assistance with the NCEM microscopes and software. Atomic coordinates for simulated *a*-Ta were provided by Jun Ding.

© Author(s) 2020

DATA AVAILABILITY

The data that support the findings of this study are openly available in Zenodo at https://doi.org/10.5281/zenodo.3836640, Ref. 34.

REFERENCES

[1] A. Bubenzer, B. Dischler, G. Bandt, and P. Koidl, "RF-plasma deposited amorphous hydrogenated hard carbon thin films: Preparation, properties, and applications," J. Appl. Phys. **54**, 4590 (1983).
[2] Y. He, X. Yu, Y. Wang, H. Li, and X. Huang, "Alumina–coated patterned amorphous silicon as the anode for a lithium–ion battery with high coulombic efficiency," Advanced Materials **23**, 4938–4941 (1983).
[3] K. Nomura, H. Ohta, A. Takagi, T. Kamiya, M. Hirano, and H. Hosono, "Room-temperature fabrication of transparent flexible thin-film transistors using amorphous oxide semiconductors," Nature **432**, 488–492 (2004).
[4] B. Shyam, K. H. Stone, R. Bassiri, M. M. Fejer, M. F. Toney, and A. Mehta, "Measurement and modeling of short and medium range order in amorphous Ta_2O_5 thin films," Sci. Rep. **6**, 32170 (2016).
[5] A. R. Yavari, J. Lewandowski, and J. Eckert, "Mechanical properties of bulk metallic glasses," MRS Bull. **32**, 635–638 (2007).
[6] S. Nakhmanson, P. Voyles, N. Mousseau, G. Barkema, and D. Drabold, "Realistic models of paracrystalline silicon," Phys. Rev. B **63**, 235207 (2001).
[7] D. L. Williamson, "Nanostructure of a-Si:H and related materials by small-angle x-ray scattering," MRS Proc. Libr. Arch. **377**, 251 (1995).
[8] G. Morell, R. S. Katiyar, S. Z. Weisz, H. Jia, J. Shinar, and I. Balberg, "Raman study of the network disorder in sputtered and glow discharge a–Si:H films," J. Appl. Phys. **78**, 5120–5125 (1995).
[9] P. Voyles and D. Muller, "Fluctuation microscopy in the STEM," Ultramicroscopy **93**, 147–159 (2002).
[10] C. Ophus, "Four-dimensional scanning transmission electron microscopy (4D-STEM): From scanning nanodiffraction to ptychography and beyond," Microsc. Microanal. **25**, 563–582 (2019).
[11] S. Hilke, H. Rösner, D. Geissler, A. Gebert, M. Peterlechner, and G. Wilde, "The influence of deformation on the medium-range order of a Zr-based bulk metallic glass characterized by variable resolution fluctuation electron microscopy," Acta Mater. **171**, 275–281 (2019).
[12] A. C. Y. Liu, M. J. Neish, G. Stokol, G. Buckley, L. Smillie, M. D. de Jonge, R. Ott, M. Kramer, and L. Bourgeois, "Systematic mapping of icosahedral short-range order in a melt-spun $Zr_{36}Cu_{64}$ metallic glass," Phys. Rev. Lett. **110**, 205505 (2013).
[13] D. Henderson, M. Brodsky, and P. Chadhauri, "Simulation of structural anisotropy and void formation in amorphous thin films," Appl. Phys. Lett. **25**, 641–642 (1974).
[14] D. Kirk, A. Kohn, K. B. Borisenko, C. Lang, J. Schmalhorst, G. Reiss, and D. J. H. Cockayne, "Structural study of amorphous CoFeB thin films exhibiting in-plane uniaxial magnetic anisotropy," Phys. Rev. B **79**, 014203 (2009).
[15] H. Windischmann, "Intrinsic stress in sputter-deposited thin films," Crit. Rev. Solid State Mater. Sci. **17**, 547–596 (1992).
[16] D. Hardwick, "The mechanical properties of thin films: A review," Thin Solid Films **154**, 109–124 (1987).
[17] X.-D. Wang, H.-F. Wang, B. Chen, Y.-P. Li, and Y.-Y. Ma, "A model for thickness effect on the band gap of amorphous germanium film," Appl. Phys. Lett. **102**, 202102 (2013).
[18] T. Li, L. Bayu Aji, T. Heo, M. Santala, S. Kucheyev, and G. Campbell, "Effect of medium range order on pulsed laser crystallization of amorphous germanium thin films," Appl. Phys. Lett. **108**, 221906 (2016).
[19] C. Gammer, C. Ophus, T. C. Pekin, J. Eckert, and A. M. Minor, "Local nanoscale strain mapping of a metallic glass during in situ testing," Appl. Phys. Lett. **112**, 171905 (2018).
[20] L. Tian and C. Volkert, "Measuring structural heterogeneities in metallic glasses using transmission electron microscopy," Metals **8**, 1085 (2018).
[21] T. C. Pekin, J. Ding, C. Gammer, B. Ozdol, C. Ophus, M. Asta, R. O. Ritchie, and A. M. Minor, "Direct measurement of nanostructural change during in situ deformation of a bulk metallic glass," Nat. Commun. **10**, 2445 (2019).
[22] Y. Deng, R. Zhang, T. C. Pekin, C. Gammer, J. Ciston, P. Ercius, C. Ophus, K. Bustillo, C. Song, S. Zhao *et al.*, "Functional materials under stress: In situ TEM observations of structural evolution," Adv. Mater. **32**, 1906105 (2019).
[23] J. Ding *et al.*, "Second-nearest-neighbor correlations from connection of atomic packing motifs in metallic glasses and liquids," Sci. Rep. **5**, 17429 (2015).
[24] C. Ophus, "A fast image simulation algorithm for scanning transmission electron microscopy," Adv. Struct. Chem. Imaging **3**, 13 (2017).
[25] A. Pryor, C. Ophus, and J. Miao, "A streaming multi-GPU implementation of image simulation algorithms for scanning transmission electron microscopy," Adv. Struct. Chem. Imaging **3**, 15 (2017).
[26] S. E. Zeltmann, A. Müller, K. C. Bustillo, B. H. Savitzky, A. M. Minor, and C. Ophus, "Improved 4D-STEM strain mapping precision using patterned probes," Microsc. Microanal. **25**, 1958–1959 (2019).
[27] ScottLab UC Berkeley, see https://github.com/ScottLabUCB/FEM for "FEM, 2019."
[28] B. H. Savitzky, L. A. Hughes, S. E. Zeltmann, H. G. Brown, S. Zhao, P. M. Pelz, E. S. Barnard, J. Donohue, L. R. DaCosta, T. C. Pekin *et al.*, "py4DSTEM: A software package for multimodal analysis of four-dimensional scanning transmission electron microscopy datasets," arXiv:2003.09523 (2020).
[29] F. Irgens, *Continuum Mechanics* (Springer, 2008).
[30] M. Treacy, J. Gibson, and P. Keblinski, "Paracrystallites found in evaporated amorphous tetrahedral semiconductors," J. Non-Cryst. Solids **231**, 99–110 (1998).
[31] J. Hwang and P. Voyles, "Variable resolution fluctuation electron microscopy on Cu-Zr metallic glass using a wide range of coherent STEM probe size," Microsc. Microanal. **17**, 67–74 (2011).
[32] T. Daulton, K. Bondi, and K. Kenneth, "Nanobeam diffraction fluctuation electron microscopy technique for structural characterization of disordered materials—Application to $Al_88 - xY_7Fe_5Ti_x$ metallic glasses," Ultramicroscopy **110**, 1279–1289 (2010).
[33] S. N. Bogle, P. M. Voyles, S. V. Khare, and J. R. Abelson, "Quantifying nanoscale order in amorphous materials: Simulating fluctuation electron microscopy of amorphous silicon," J. Phys. **19**, 455204 (2007).
[34] E. R. Kennedy, "Tilted fluctuation electron microscopy data from simulated and deposited amorphous Ta," Zenodo. https://doi.org/10.5281/zenodo.3836640

© Author(s) 2020